Direct laser ion acceleration and above-threshold ionization at intensities from 10^{21} W/cm^2 to 3×10^{23} W/cm^2

A. Yandow,[1] T. Toncian,[1,2] and T. Ditmire[1]

[1]*Center for High Energy Density Science, 2515 Speedway RLM 12.204, Austin, Texas 78712, USA*

[2]*Institute of Radiation Physics, Helmholtz-Zentrum Dresden-Rossendorf, 01328 Dresden, Germany*

(Received 4 September 2019; published 11 November 2019)

Calculations on the dynamics of ions and electrons in near-infrared laser fields at intensities up to 3×10^{23} W/cm^2 are presented. We explore the acceleration of ions in a laser focus by conservation of canonical momentum during ionization events and by the ponderomotive force in the $f/1$ focal geometry required to reach such intensity. At intensities exceeding 10^{23} W/cm^2, highly charged ions are expelled from the laser focus before they can interact with the laser pulse at peak intensity, decreasing the predicted ionization yields of deeply bound states. We consider the interaction of a tightly focused, $f/1$ laser pulse with krypton at an intensity of 3×10^{23} W/cm^2 and a pulse duration of 140 fs. We find that the ions and electrons are accelerated to energies in excess of 2 MeV/nucleon and 1.4 GeV, respectively. Ponderomotive expulsion of the parent ions decreases the total number of ultrarelativistic above-threshold ionization electrons produced by tunneling ionization from the K-shell states of krypton but does not change their energy spectrum.

DOI: 10.1103/PhysRevA.100.053406

I. INTRODUCTION

Above-threshold ionization (ATI), first observed by Agostini *et al.* in 1979 [1], is the fundamental response of an atomic system to a strong laser field and the dominant laser energy absorption mechanism in low-density plasmas. When the density of photons becomes high enough, ATI can be treated as a quasiclassical, two-step process: the bound electron is freed by adiabatic tunneling and the continuum dynamics can be found by integrating the Lorentz force equations. The two-step model of ATI has been used to explain high-harmonic generation in gases [2,3] and nonsequential double ionization (NSDI) [4,5]. Measurements of the ATI electron energy spectrum and angular distribution provide direct evidence that tunneling ionization dominates in infrared laser fields above 10^{15} W/cm^2 [6,7]. Laser intensities currently exceed 2×10^{22} W/cm^2 [8,9] and now approach 10^{23} W/cm^2, a regime where ATI offers a method of accelerating electrons to GeV energies over a few microns.

Free electron dynamics in near-infrared laser fields become relativistic at intensities above 10^{18} W/cm^2. The trajectories of electrons liberated by tunneling ionization in these fields are folded forward by the laser magnetic field, and the electrons are observed to gain momentum in the laser forward direction [10]. Despite the onset of relativistic free electron motion, precision measurements of the ionization rates of argon at intensities up to 2×10^{19} W/cm^2 have agreed with the nonrelativistic Ammosov-Krainov-Delone and Perelomov-Popov-Terent'ev (ADK-PPT) tunneling model of ionization [11]. Although ionization channels involving inelastic rescattering are suppressed by relativistic electron drift in the continuum [12], it is less clear how relativistic laser-electron interactions affect the primary ionization process. The laser magnetic field is thought to play a role in stabilizing bound states by giving the electron a nonzero momentum component transverse to the tunneling path, effectively increasing the height of the tunneling barrier [13]. However, numerical treatment of ionization as an ensemble of classical electron orbits demonstrated that the inclusion of the laser magnetic field has negligible effects on the ionization rates at intensities up to 10^{23} W/cm^2 [14]. Tunneling rate models for hydrogenlike ions that use Dirac wave functions predict the ionization rate will be $\sim 1/3$ of the nonrelativistic rate above 10^{23} W/cm^2 [15], but the corrections from the laser magnetic field are negligible [16]. Precision measurements of highly charged ion yields and ATI electron energy spectra are needed to verify the magnitude of expected relativistic corrections.

In this article we numerically investigate the ionization and electron dynamics in ultraintense laser fields that will be available with hybrid OPCPA-Nd:glass systems scheduled to come online in the near future [17]. We employed numerical methods that allowed us to model tunneling ionization and calculate ATI electron energy spectra without neglecting the motion of the parent ions in the laser field. The ions will acquire energy from their interaction with the laser field, which has been numerically explored as a method for creating high-energy proton pulses for cancer therapy [18]. When laser intensity exceeds 10^{23} W/cm^2 in the $f/1$ focal geometry required to reach this intensity with a 10-PW-class laser, the ponderomotive force expels the ions before they can interact with strongest laser field. For highly charged krypton ions in a laser focus, we demonstrate that ponderomotive ion expulsion will substantially reduce the number of K-shell ionization events. Simulations of the ATI electron dynamics show evidence of two dominant electron acceleration mechanisms for the highest-energy ATI electrons. We conclude that direct laser ion acceleration (DLIA) will necessitate the development of novel

experimental techniques to measure ionization rates when intensity exceeds 10^{21} W/cm^2.

II. ION DYNAMICS

The physics of direct laser ion acceleration is analogous to the acceleration of ATI electrons in nonrelativistic, near-infrared laser fields. We can extend the quasiclassical two-step model of Corkum *et al.* [6] to approximate ion energy contributions from two sources: residual drift that arises from conservation of canonical momentum in the laser field at each ionization event and from ponderomotive acceleration. Assuming a sequential tunneling ionization process, nonrelativistic ion motion, and negligible ponderomotive force on the ion, we can express the energy as

$$E_{\text{drift}} \approx \frac{1}{2m\omega^2}\left[\sum_{q=1}^{q_{\max}} E(t_q)\sin(\phi_q)\right]^2 \tag{1}$$

in a linearly polarized laser field, where $E(t_q)$ is the laser electric field amplitude and ϕ_q is the laser phase at the time of the qth ionization event. The ion residual drift energy spectrum can only be calculated numerically as the energy spectrum includes information about the laser phase and field strength at every ionization event, and therefore the energy spectrum depends strongly on the target ion species and its electronic shell structure.

For the tight $f/1$ focal geometries considered in this paper, the ponderomotive energy contribution dominates the residual drift energy at intensities above 10^{21} W/cm^2. One can approximate the ponderomotively ejected ion energy as

$$\begin{aligned} E_{\text{pond}} &\approx \frac{1}{2m}\left[\int_{-\infty}^{\infty} \nabla U_p(\mathbf{x}(t), t, q(t))dt\right]^2 \\ &= \frac{1}{32m^3\omega^4}\left[\int_{-\infty}^{\infty} q(t)^2 \nabla \mathbf{E}(\mathbf{x}(t), t)^2 dt\right]^2, \end{aligned} \tag{2}$$

where $U_p = q^2E^2/4m\omega^2$ is the ion ponderomotive potential and $q(t)$ is the ion charge as a function of time. The details of ponderomotive ion ejection are complex, and the final energy depends on charge state history, laser intensity, spot size, pulse duration, and initial position within the laser focus, and thus no general formula for final ion energy exists. Simulations of the ion dynamics illustrate both residual drift and ponderomotive DLIA when considering laser-ion interactions on 10-PW-class laser systems.

We simulate the ion dynamics by numerically integrating the Lorentz force equations using the Runge-Kutta-Felberg method. We neglect space-charge fields in our simulations, and they can be ignored when considering skimmed effusive atomic beams with densities on the order of 10^{11} cm^{-3} and a diameter of $\sim$1 mm. The atom is neutral before arrival of the laser pulse, and at each time step, the probability of ionization is calculated using the ADK-PPT tunneling ionization rate [19,20]. We assume the single active electron approximation, neglecting collective tunneling and recollision effects, and increment the charge state using straightforward Monte Carlo methods. The ion charge state histories can be reproduced using ionization potentials from Kelly and Harrison [21] for krypton and the NIST Atomic Spectral Database for all other elements [22]. We model the laser field as a Gaussian focus, and we include nonparaxial corrections up to fifth order in the diffraction angle [23].

Figures 1 and 2 present simulated ion energy spectra for argon and krypton. The peak intensities are chosen to be the barrier suppression intensity (BSI) [24] of the hydrogenlike ion charge states. Numerical solution of the time-dependent Schrödinger equation demonstrates that the ADK-PPT model likely overestimates the tunneling probability as the barrier suppression regime is approached [25]. However, for highly charged ions, the probability of ionization by tunneling will be significant before the barrier suppression intensity is reached, so these corrections can typically be ignored [26]. The estimated pulse duration below which barrier suppression effects must be considered is on the order of 5 fs for the ionization of Ar^{17+} [27], much shorter than the 140-fs pulse duration we consider throughout this article. The ADK-PPT model and the single electron approximation may be less accurate when considering the ionization events in the low-intensity leading edge of the laser pulse, but they will provide a better estimate of the charge state history than assuming a preionized target. We randomly choose the initial position of the neutral atom within the laser confocal region and propagate the laser pulse through, repeating for 10^5 trials. The laser central wavelength is 1057 nm throughout this article.

Figures 1(a) and 1(b) show the calculated energy spectra of argon in $f/10$ and $f/1$ focal geometries, which we take to have $1/e^2$ diameters of 30 and 3 μm, respectively. The peak laser intensity is 4.7×10^{21} W/cm^2, which can be attained by a 10-PW-class laser system in the larger focus. Residual drift ion energy dominates in the $f/10$ geometry for Ar^{17+} and Ar^{18+}, yielding an exponential distribution of ejected ion energies. The large gap in calculated ion energy between Ar^{16+} and the higher charge states reflects the large difference in ionization potential (and hence, the BSI) between the L-shell and K-shell electrons of argon. The ponderomotive force dominates the dynamics of ions expelled from the $f/1$ focus, and ion energy reflects the strength of the ponderomotive force at each ion's initial position in the focus. Residual drift is necessary to explain the hot ion tail of Ar^{18+} in the $f/1$ geometry. Figure 1(c) shows the azimuthal angular distribution of Ar^{18+} ejected from each focus, confirming that ions accelerated by residual drift will be expelled preferentially along the laser polarization direction while ponderomotively accelerated ions will be expelled radially. Figure 2 shows the energy spectrum of krypton ions expelled from an $f/1$ focus where the peak laser intensity is 3×10^{23} W/cm^2. The peak krypton ion energy is in excess of 200 MeV. We will show that, in this ultraintense regime, the highest-energy ejected ions will gain nearly the full ponderomotive energy.

Ponderomotive DLIA can be divided into long- and short-pulse regimes. In both regimes, the ion experiences a ponderomotive force $f_p = -\nabla U_p \sim -U_p/w_o$. When the laser pulse duration is much shorter than the timescale on which the ion leaves the focus, a small amount of the ponderomotive potential is converted to kinetic drift energy. Assuming a stationary ion, integrating the ponderomotive force over the laser pulse duration τ_p gives an impulse $\Delta p \sim -\frac{U_p\tau_p}{w_o}$, yielding a quadratic ion energy scaling with peak intensity. A calculation

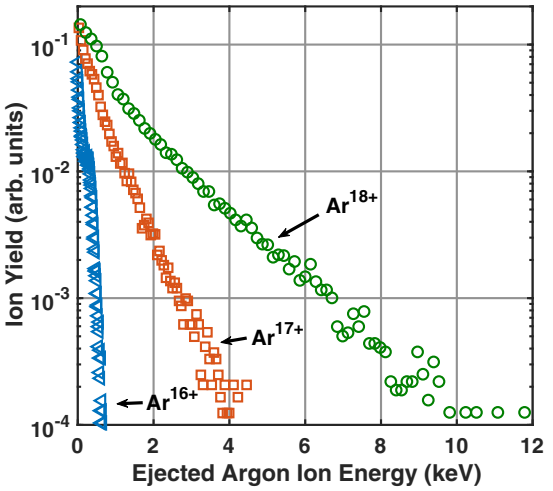

(a)

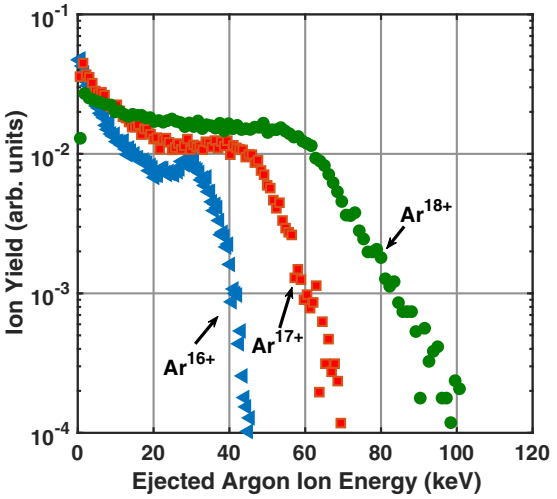

(b)

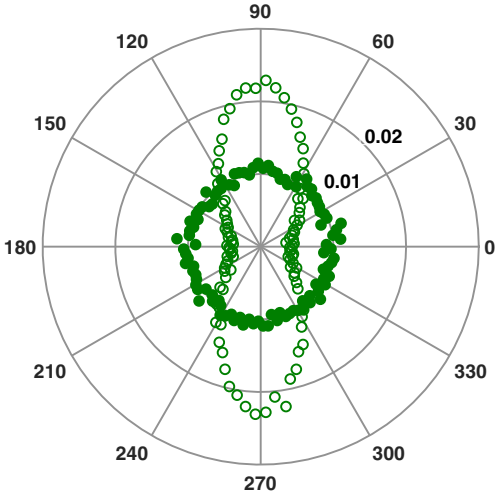

(c)

FIG. 1. Energy spectra of argon ions ejected from a laser focus with peak intensity of 4.7×10^{21} W/cm^2 from (a) a 30-μm focal diameter (open markers) and (b) 3-μm focal diameter (closed markers). Blue triangles, red squares, and green circles represent Ar^{16+}, Ar^{17+}, and Ar^{18+}, respectively. (c) Comparison of angular distribution (arb.) of Ar^{18+} in both geometries.

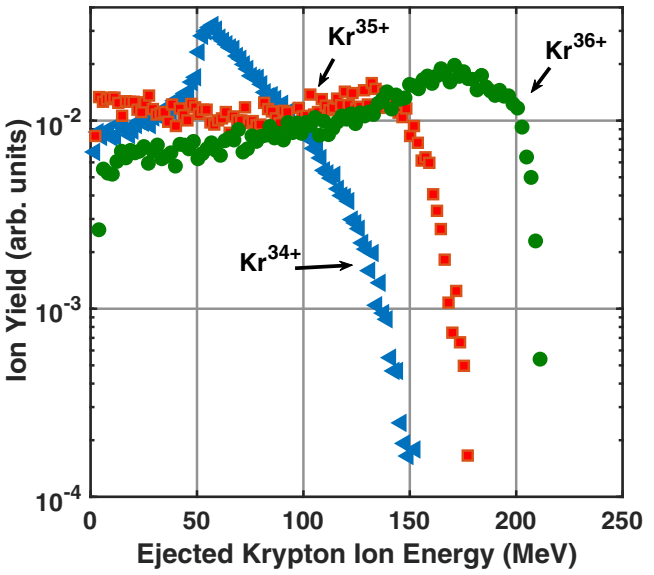

FIG. 2. Energy spectra of krypton ions ejected from the laser focus with peak intensity of 3×10^{23} W/cm^2 and a 3-μm focal diameter. Blue triangles, red squares, and green circles represent Kr^{34+}, Kr^{35+}, and Kr^{36+}, respectively. The peak at around 60 MeV for Kr^{34+} is an artifact of the simulation boundaries, which exclude the large volume of lower-energy Kr^{34+} produced several Rayleigh ranges away from the focal plane.

assuming a Gaussian spatial mode and temporal profile as well as a constant ion charge q gives a maximum energy of

$$E_{\mathrm{ion},sp} = \frac{\pi}{8\ln(2)\exp(1)} \frac{q^4}{\omega^4 c^2 \epsilon_o^2 m^3} \left(\frac{I_o \tau_p}{w_o}\right)^2 \qquad (3)$$

due to ponderomotive acceleration in the short-pulse regime, where τ_p is the intensity FWHM pulse duration, I_o is the peak laser intensity, and w_o is the beam waist. When the laser pulse duration becomes comparable to the ejection timescale (long-pulse regime), we expect a significant fraction of the ion ponderomotive energy, which scales linearly with intensity, is converted to kinetic drift energy. An approximate ion ejection timescale $\tau_{ej} \approx w_o\sqrt{2m/U_p}$ can be derived from the ponderomotive model. For an $f/1$ focus, this timescale is on the order of 1 ps for hydrogenlike argon at its BSI but is ~120 fs for hydrogenlike krypton at its BSI.

The mechanisms of DLIA discussed in this article closely resemble the nonrelativistic picture of ATI, with the key difference that the ponderomotive dynamics often dominate residual drift even in the short-pulse regime. Residual drift plays a minor role because the ion charge-to-mass ratio does not change much during ionization events occurring at the peak laser field strength and the canonical momenta gained during successive ionization events can cancel each other. The interplay between ponderomotive acceleration and residual drift acceleration depends strongly on the ion species and its trajectory, so the transition between residual drift and short-pulse ponderomotive dynamics can only be predicted numerically. The ponderomotive impulse model presented for the short-pulse ponderomotive regime closely parallels the surfing picture presented by Bucksbaum *et al.*, where the ponderomotive potential was observed to accelerate (or

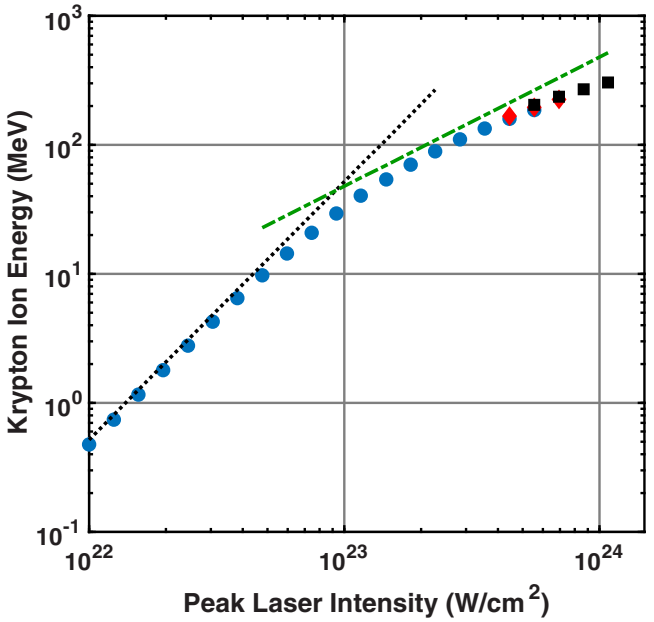

FIG. 3. Average energy of 500 krypton ions originating from $(w_o/2, 0, 0)$ for different peak laser intensities. Peak laser intensity is defined at (0, 0, 0). Blue circles indicate Kr^{34+}, red diamonds indicate Kr^{35+}, and black squares indicate Kr^{36+}. The black dotted line and the green dashed line are the short-pulse maximum energies [Eq. (3)] or ponderomotive energy for a Kr^{34+} ion, respectively. The focal spot $1/e^2$ diameter is 3 μm.

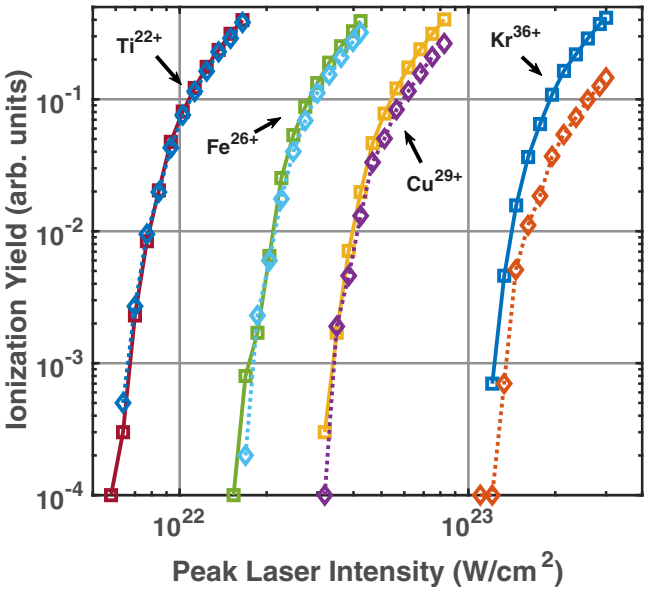

FIG. 4. Ionization probability for hydrogenlike states of ions (left to right: Ti^{21+}, Fe^{25+}, Cu^{28+}, and Kr^{35+}) in a laser focus as laser intensity increases above 10^{23} W/cm^2, including (diamonds, dotted curves) and excluding (squares, solid curves) ion motion. Color included for clarity. The focal spot $1/e^2$ diameter is 3 μm.

decelerate) nonrelativistic ATI electrons crossing the focal volume of a laser field between the ATI electron source and detector [28].

We confirmed the ponderomotive ejection timescale estimate by simulating 500 krypton ions originating from the point of strongest ponderomotive force in a laser focus with a $1/e^2$ diameter of 3 μm. The averages of these ion energies are presented in Fig. 3. As the peak laser intensity in the focus increases, the ponderomotive force on the ion also increases. When intensity exceeds 10^{23} W/cm^2, the ions are expelled from the focus on the timescale of the laser pulse duration, gaining a significant fraction of the ion ponderomotive energy at its initial position. This short- to long-pulse regime transition causes the change in ion energy scaling with intensity from quadratic to linear seen in Fig. 3 at 10^{23} W/cm^2. In the short-pulse ponderomotive DLIA regime, the ions originating from the point of strongest ponderomotive force in the focus will have the highest energy, and we observe agreement with Eq. (3). As 10^{24} W/cm^2 is approached, the scaling becomes sublinear because the ion is expelled from the focus before the peak intensity is reached.

Calculating ionization yields in the long-pulse DLIA regime is complicated by the fact that the number of ions in the focal volume does not remain constant over the laser pulse duration. The ions will be expelled from the laser focus before being ionized further by the peak strength of the laser field, and we expect calculations including and excluding ion motion to differ substantially when $\tau_p \sim \tau_{ej}$. We calculate the ionization yields by integrating 10^4 initial atom positions distributed over a fixed focal volume, bounded by the isointensity shell where the probability of K-shell ionization is greater than 0.05 for stationary ions. Simulated ion yields, including and excluding the ion motion, are given in Fig. 4. An increasing difference between the stationary and mobile ion models is observed as the laser intensity approaches 10^{23} W/cm^2. Mobile and immobile yields for hydrogenlike krypton differ by a factor of ~3, demonstrating that ion motion must be accounted for when calculating ionization yields. We expect that the ion yield decrease due to ponderomotive ion ejection will be comparable to the decrease caused by relativistic corrections to the ionization rates.

III. ELECTRON DYNAMICS

The final energies of ATI electrons depend strongly on the laser phase at the instant of ionization [7]. In the ultrarelativistic regime ($I > 10^{21}$ W/cm^2), the energy spectrum of ATI electrons is also sensitive to target ion position in the laser focus. Numerical studies of ATI electrons produced by the ionization of hydrogenlike argon suggest the highest-energy electrons originate from ions located from the front and sides of the confocal region [29,30]. If the most energetic ATI electrons originate from the edges of the focal volume, where the ponderomotive force on the ions is strongest, we expect a disproportionate reduction in the number of high-energy ATI electrons produced because their parent ions will be ejected from the focus before ionization. We therefore simulated the dynamics of ATI electrons produced by the ionization of hydrogenlike, highly charged ions in the laser focus.

The electron initial conditions were generated by simulating the ion dynamics in the focal volume using the same method for calculating the ionization yields described in the previous section. Each ion velocity, position, and time is

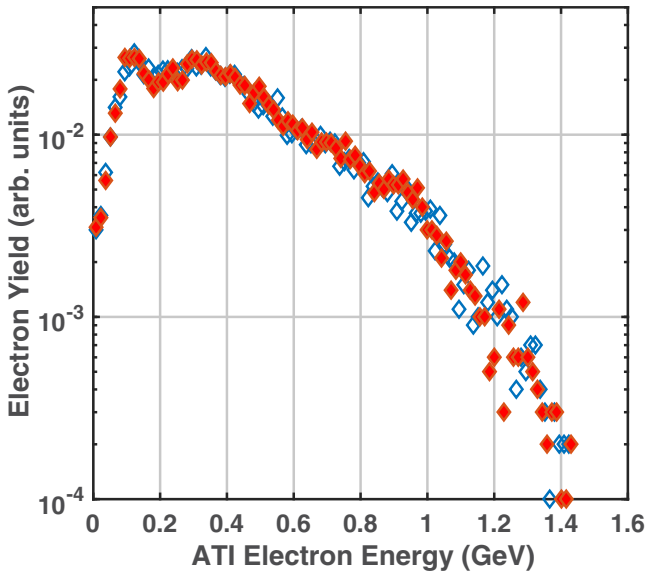

FIG. 5. ATI electron energy spectra for electrons produced by ionization of Kr^{35+} integrated over the focal volume. Electron initial conditions are calculated by simulation of immobile (closed diamonds, red) or mobile (open diamonds, blue) krypton ions in the focus. The peak laser intensity is 3×10^{23} W/cm^2 and focal spot $1/e^2$ diameter is 3 μm.

recorded at the instant the hydrogenlike state is ionized. The electrons are born into the laser field at rest with respect to their parent ions. Unless explicitly mentioned otherwise, the effects of ion motion are included when calculating the initial conditions. The Coulomb field is neglected after ionization, and the electron dynamics are found by integrating the equations of motion using a modified seventh-order Dormand-Prince scheme [31]. The equations of motion, given below, are the Lorentz force equation with a correction added for the leading term of the Landau-Lifshitz radiation friction force [32,33]:

$$\begin{aligned}\frac{d\mathbf{p}}{dt} &= -e\left(\mathbf{E}+\frac{\mathbf{v}}{c}\times\mathbf{B}\right)\\ &+\frac{2}{3}r_c^2\left\{\left[\left(\mathbf{E}+\frac{\mathbf{v}}{c}\times\mathbf{B}\right)\times\mathbf{B}+\left(\frac{\mathbf{v}}{c}\cdot\mathbf{E}\right)\mathbf{E}\right]\right.\\ &\left.-\gamma^2\left[\left(\mathbf{E}+\frac{\mathbf{v}}{c}\times\mathbf{B}\right)^2-\left(\frac{\mathbf{v}}{c}\cdot\mathbf{E}\right)^2\right]\frac{\mathbf{v}}{c}\right\},\end{aligned} \tag{4}$$

where $r_c = e^2/m_e c^2$ is the classical electron radius and γ is the Lorentz factor. The radiation reaction correction decreases the final energy of the highest-energy electron we simulated by approximately 0.2%. 10^4 unique electron initial conditions were used for each simulation. The laser polarization is oriented along the x axis, and the laser forward direction is oriented along the positive z axis.

Figure 5 shows nearly identical ATI electron energy spectra for from ionization of hydrogenlike krypton at an intensity of 3×10^{23} W/cm^2 when ion motion is ignored (closed markers) or included (open markers) when generating the initial electron conditions. ATI simulations were performed over two decades of laser intensity, and the parent ion positions

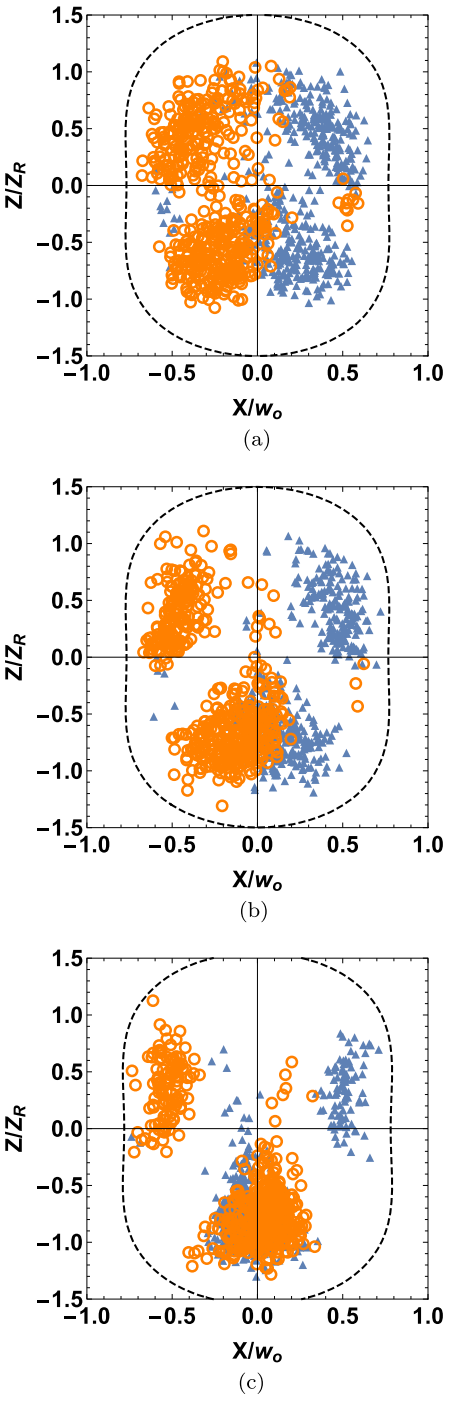

FIG. 6. Initial positions of the 10% highest-energy ATI electrons produced by (a) Ar^{17+} at 4.7×10^{21} W/cm^2, (b) Ti^{21+} at 1.6×10^{22} W/cm^2, and (c) Kr^{35+} at 3×10^{23} W/cm^2. Open orange circles denote negative E_x, solid blue triangles denote positive E_x. The focal spot $1/e^2$ diameter is 3 μm. The black dashed curve represents the focal volume boundary containing all atoms (before arrival of the laser pulse) in the simulation.

at the moment of ionization were recorded. Figure 6 shows the ion positions from which the 10% most energetic ATI electrons originate, projected onto the XZ plane, for three ion species (Ar^{17+}, Ti^{21+}, and Kr^{35+}). The peak laser intensities in the Gaussian focus and temporal envelope are chosen to

be their respective barrier suppression intensities. The color (shape) of the markers indicates the direction of the paraxial laser field E_x at the moment of ionization. A transition in the electron acceleration mechanisms is evidenced by the development of three distinct, compact regions in the focus where the high-energy electrons are generated. At an intensity of 3×10^{23} W/cm^2, the vast majority of the high-energy ATI electrons originate from ions concentrated along the laser axis in the back of the confocal region where the ponderomotive force is weaker than it is at the beam waist. These ions are not likely to be expelled more quickly than other ions in the focus, explaining the consistency between the simulations excluding and including ion motion seen in Fig. 5.

The presence of these three distinct regions leads us to identify two ultrarelativistic electron acceleration mechanisms where the longitudinal electric field E_z plays an important role. The first-order nonparaxial laser fields are oriented along the laser propagation direction and must be included to ensure the electric and magnetic laser fields remain divergence-free and therefore satisfy Maxwell's equations. The first-order nonparaxial magnetic field was shown to be essential for a correct description of the ponderomotive force by Quesnel and Mora, but the first-order nonparaxial electric field plays little role in the electron dynamics at softly relativistic intensity [34]. However, E_z will do work on the electron in the ultrarelativistic regime, when it points nearly parallel to the electron velocity. The work provided by the longitudinal electric field substantially reduces the calculated energies of ultrarelativistic ATI electrons because it dephases these electrons from the paraxial laser electric field [35]. We refer to the mechanism accelerating electrons from the back of the confocal region as rephasing acceleration (RA) and the mechanism accelerating electrons out of the front of the focus as direct injection acceleration (DIA).

Electrons accelerated by either mechanism accelerate to nearly the speed of light in the laser forward direction in a small fraction of a laser cycle. Although the magnitude of the nonparaxial electric field directed along the laser propagation direction is lower than the paraxial fields by an order of magnitude, it contributes substantially to the rate of electron energy change $dE/dt \; \alpha \; \mathbf{E} \cdot \mathbf{v}$ as $v_z/v_x \approx \sqrt{\gamma/2}$ [35]. The trajectories of two test electrons, one accelerated by DIA and one by RA, were calculated as they exited the confocal region nearly parallel to the z axis. Figure 7(a) shows the Lorentz factor γ for the RA electron (solid blue) and the DIA electron (dashed-dotted green) with all fields included. The same trajectories with all nonparaxial fields excluded with the exception of the first-order nonparaxial magnetic field are displayed for comparison (dashed red for the RA mechanism, dotted black for the DIA mechanism). Dephasing from the paraxial field in this scenario is driven only the superluminal phase velocity of the focused beam [36], leading to lower electron energy gain and loss rates. Figure 7(b) shows both the normalized E_x (no markers) and E_z (open squares) experienced by the two test electrons when the nonparaxial corrections are included. The signs of the fields in Fig. 7(b) provide a qualitative description of the acceleration mechanisms.

For the DIA mechanism, the electron is born in the front of the confocal region. The sign of E_x, as noted in Fig 6(c),

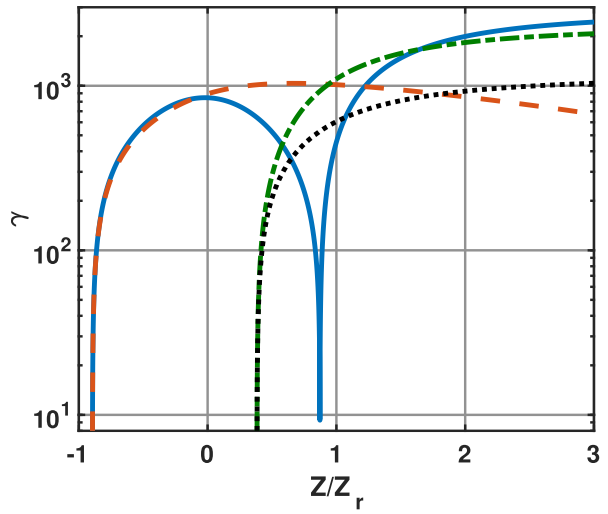

(a)

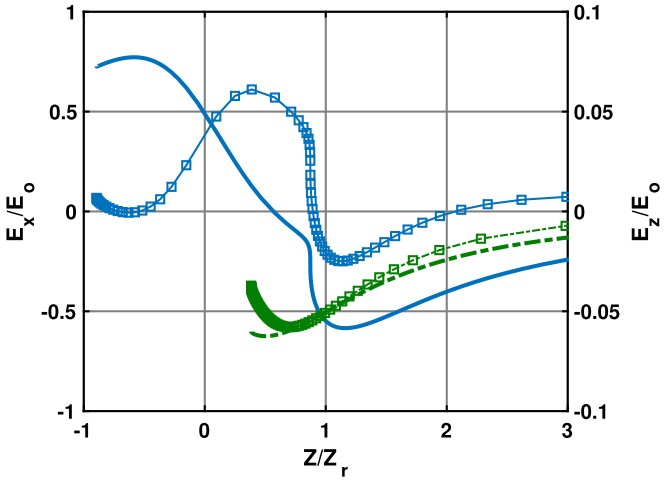

(b)

FIG. 7. (a) Test electron γ as it travels through focus for representative initial conditions for RA (solid blue, negative z origin) and DIA (dashed-dotted green, positive z origin). Red dashed lines and black dotted lines represent identical initial conditions with the only first-order nonparaxial magnetic correction included. (b) Electric fields acting on the test electrons. Color scheme is the same as (a) for E_x (left scale). E_z (right scale) is represented by corresponding line style with open square markers. Electron motion is very nearly parallel to the z axis.

immediately accelerates the electron toward the z axis in both DIA regions while E_z is negative, as seen in Fig 7(b). The paraxial magnetic field folds the electron trajectories toward the laser forward direction, and the electron remains nearly in phase with the paraxial laser field as it gains energy from E_z. In the RA mechanism, the electron loses energy to work done by E_z faster than it gains energy from work done by E_x, and begins to decelerate before the sign of E_x changes. Complete deceleration is averted by the longitudinal magnetic field, which exerts a force ($\alpha \; v_\perp B_z$) in the XY plane, reversing the electron motion in the x direction so it can gain energy from E_x without completely decelerating. These electrons gain more energy than the initially stationary DIA electrons "born" in

the front of the confocal region, because they gain energy at a higher rate from the paraxial field ($dE/dt \propto cE_x$) due to their relativistic velocity at the instant of acceleration.

IV. DISCUSSION

While our observation of the highest-energy ATI electrons originating from the back of the confocal region is unexpected, it does not necessarily contradict the results of previous studies. We do not find qualitative agreement with Pi *et al.* for origin positions of the highest-energy ATI electrons from Ar^{17+} [30], but we emphasize that the final electron energy is much more sensitive to the laser phase at the moment of ionization than it is to initial position in the focus. The over-the-barrier ionization model used in their paper will yield a different distribution of initial phases than the quantum ADK model, which can make direct comparison of our results difficult. We also restricted our analysis of initial electron positions to an intensity regime the ion yield is not strongly saturated. At higher intensities where the ion yield is strongly saturated, electrons will originate from a larger volume of the focus and the distribution of preferred initial positions may change. Other numerical studies of free electron acceleration by few-cycle, petawatt, radially polarized pulses [37] and fully nonparaxial linearly polarized pulses [36] show high-energy scattered electrons originating from positions the back of the confocal region.

DLIA poses a formidable challenge to ionization rate experiments at intensities above 10^{21} W/cm^2. Even in focal geometries where ponderomotive acceleration can be neglected, canonical momentum conservation accelerates the ions to keV energies. Wiley-McLaren time-of-flight methods, which were used to measure ionization yield in virtually all previous ionization rate experiments with noble gases [11,24,38], will not be able to capture all the ions nor will they have sufficient resolution to resolve the closely spaced charge-to-mass ratio peaks when the ions have the broad energy spectra we predict. Ionization yield measurements for hydrogenlike and heliumlike charge states of argon and krypton will have to be inferred from the high-energy ATI electrons ejected from the laser focus. ATI electrons generated by tunneling from the K shell will typically have at least an order of magnitude higher peak energy than ATI electrons originating from the L shell. Ponderomotive expulsion of ions from the laser focus will not disproportionately reduce the number of high-energy ATI electrons produced when the ion yield is not saturated.

The techniques recently proposed by Ciappina *et al.* [26] to determine peak laser intensity by measuring relative yields of highly charged ions produced in the focus will lose substantial intensity resolution if the only experimental observable is the relative ATI electron yields from different atomic shells rather than relative yields of ion charge states within those shells. Further systematic study of ATI electron energies produced by each charge state will be necessary to determine the limit of intensity resolution and will aid the selection of appropriate target atoms for different intensities. The rate equation model of ionization will overestimate the yield of high charge states and thus underestimate the laser intensity when the long-pulse DLIA regime is reached.

DLIA will substantially reduce the number of K-shell ionization events in a tightly focused laser beam at intensities greater than 10^{23} W/cm^2 and must be included to accurately calculate the expected number of ionization events. Shorter laser pulses (<25 fs) can mitigate the effect of DLIA on the ionization yield, but ionization yields do not compare well with indirect intensity measurements inferred from the focal spot size and pulse duration diagnostics due to B-integral accumulation in the diagnostic transport [39]. For longer pulses of hybrid OPCPA-Nd:glass laser systems, the intensities inferred from ionization yields and indirect measurements compare favorably [40], and measuring ionization threshold intensities above 10^{23} W/cm^2 with a longer pulse system can enable accurate cross calibration of shorter pulse systems. The electronic shell structure of the target atoms can also be studied by examining modulations in the angular distribution and energy spectrum of the ATI electrons [41,42], but these features will be washed out by the rapid intensity ramp-up of shorter pulses.

V. CONCLUSION

A complete understanding of ion and ATI electron dynamics in tightly focused, nonparaxial laser fields will be essential to study relativistic corrections to the tunneling ionization rates at intensities above 10^{23} W/cm^2. At these intensities, broad DLIA energy spectra ($E_{max} \sim 2$ MeV/nucleon) will make direct detections of ion charge states and measurement of the ionization yields extremely challenging. Future experimental studies of ionization rates at such intensity will require the development of large-area, high-dynamic-range electron detectors capable of detecting individual 100-MeV–1.5-GeV electrons expelled from the laser focus.

ACKNOWLEDGMENTS

This work was supported by the Air Force Office of Scientific Research (AFOSR) through Awards No. FA9550-14-1-0045 and No. FA9550-17-1-0264, and by the National Nuclear Security Agency (NNSA) through Award No. DE-NA0002008. A.Y. gratefully acknowledges the generous support of the Jane and Mike Downer Endowed Presidential Fellowship in Laser Physics in Memory of Glenn Bryan Focht.

[1] P. Agostini, F. Fabre, G. Mainfray, G. Petite, and N. K. Rahman, Free-Free Transitions Following Six-Photon Ionization of Xenon Atoms, Phys. Rev. Lett. **42**, 1127 (1979).

[2] P. B. Corkum, Plasma Perspective on Strong-Field Multiphoton Ionization, Phys. Rev. Lett. **71**, 1994 (1993).

[3] J. L. Krause, K. J. Schafer, and K. C. Kulander, High-Order Harmonic Generation from Atoms and Ions in the High Intensity Regime, Phys. Rev. Lett. **68**, 3535 (1992).

[4] D. N. Fittinghoff, P. R. Bolton, B. Chang, and K. C. Kulander, Observation of Nonsequential Double Ionization of Helium with Optical Tunneling, Phys. Rev. Lett. **69**, 2642 (1992).

[5] J. B. Watson, A. Sanpera, D. G. Lappas, P. L. Knight, and K. Burnett, Nonsequential Double Ionization of Helium, Phys. Rev. Lett. **78**, 1884 (1997).

[6] P. B. Corkum, N. H. Burnett, and F. Brunel, Above-Threshold Ionization in the Long-Wavelength Limit, Phys. Rev. Lett. **62**, 1259 (1989).

[7] S. J. McNaught, J. P. Knauer, and D. D. Meyerhofer, Photoelectron initial conditions for tunneling ionization in a linearly polarized laser, Phys. Rev. A **58**, 1399 (1998).

[8] G. Tiwari, E. Gaul, M. Martinez, G. Dyer, J. Gordon, M. Spinks, T. Toncian, B. Bowers, X. Jiao, R. Kupfer, L. Lisi, E. McCary, R. Roycroft, A. Yandow, G. D. Glenn, M. Donovan, T. Ditmire, and B. M. Hegelich, Beam distortion effects upon focusing an ultrashort petawatt laser pulse to greater than 10^{22} W/cm^2, Opt. Lett. **44**, 2764 (2019).

[9] J. W. Yoon, C. Jeon, J. Shin, S. K. Lee, H. W. Lee, I. W. Choi, H. T. Kim, J. H. Sung, and C. H. Nam, Achieving the laser intensity of 5.5×10^{22} W/cm^2 with a wavefront-corrected multi-PW laser, Opt. Express **27**, 20412 (2019).

[10] C. I. Moore, J. P. Knauer, and D. D. Meyerhofer, Observation of the Transition from Thomson to Compton Scattering in Multiphoton Interactions with Low-Energy Electrons, Phys. Rev. Lett. **74**, 2439 (1995).

[11] E. A. Chowdhury, C. P. J. Barty, and B. C. Walker, "Nonrelativistic" ionization of the L-shell states in argon by a "relativistic" 10^{19} W/cm^2 laser field, Phys. Rev. A **63**, 042712 (2001).

[12] M. Dammasch, M. Dörr, U. Eichmann, E. Lenz, and W. Sandner, Relativistic laser-field-drift suppression of nonsequential multiple ionization, Phys. Rev. A **64**, 061402(R) (2001).

[13] E. Yakaboylu, M. Klaiber, H. Bauke, K. Z. Hatsagortsyan, and C. H. Keitel, Relativistic features and time delay of laser-induced tunnel ionization, Phys. Rev. A **88**, 063421 (2013).

[14] P. D. Grugan, S. Luo, M. Videtto, C. Mancuso, and B. C. Walker, Classical study of ultrastrong nonperturbative-field interactions with a one-electron atom: Validity of the dipole approximation for the bound-state interaction, Phys. Rev. A **85**, 053407 (2012).

[15] N. Milosevic, V. P. Krainov, and T. Brabec, Semiclassical Dirac Theory of Tunnel Ionization, Phys. Rev. Lett. **89**, 193001 (2002).

[16] N. Milosevic, V. P. Krainov, and T. Brabec, Relativistic theory of tunnel ionization, J. Phys. B **35**, 3515 (2002).

[17] B. Rus, P. Bakule, D. Kramer, J. Naylon, J. Thoma, M. Fibrich, J. T. Green, J. C. Lagron, R. Antipenkov, J. Bartoníček, F. Batysta, R. Baše, R. Boge, S. Buck, J. Cupal, M. A. Drouin, M. Ďurák, B. Himmel, T. Havlíček, P. Homer *et al.*, ELI-beamlines: Progress in development of next generation short-pulse laser systems, Proc. SPIE **10241**, 102410J (2017).

[18] Y. I. Salamin, Z. Harman, and C. H. Keitel, Direct High-Power Laser Acceleration of Ions for Medical Applications, Phys. Rev. Lett. **100**, 155004 (2008).

[19] M. V. Ammosov, N. B. Delone, and V. P. Krainov, Tunnel ionization of complex atoms and of atomic ions in an alternating electromagnetic field, J. Exp. Theor. Phys. **64**, 1191 (1986).

[20] A. Perelomov, V. Popov, and M. Terent'ev, Ionization of atoms in an alternating electric field, J. Exp. Theor. Phys. **23**, 924 (1966).

[21] R. L. Kelly and D. E. Harrison, Jr., Ionization potentials, experimental and theoretical, of the elements hydrogen to krypton, At. Data Nucl. Data Tables **3**, 177 (1971).

[22] A. Kramida, Y. Ralchenko, J. Reader, and NIST ASD Team, NIST Atomic Spectra Database (ver. 5.6.1) [Online], Available at https://physics.nist.gov/asd [2019, October 2], National Institute of Standards and Technology, Gaithersburg, MD (2018).

[23] Y. I. Salamin, Fields of a Gaussian beam beyond the paraxial approximation, Appl. Phys. B **86**, 319 (2007).

[24] S. Augst, D. D. Meyerhofer, D. Strickland, and S. L. Chin, Laser ionization of noble gases by Coulomb-barrier suppression, J. Opt. Soc. Am. B **8**, 858 (1991).

[25] D. Bauer and P. Mulser, Exact field ionization rates in the barrier-suppression regime from numerical time-dependent Schrodinger-equation calculations, Phys. Rev. A **59**, 569 (1999).

[26] M. F. Ciappina, S. V. Popruzhenko, S. V. Bulanov, T. Ditmire, G. Korn, and S. Weber, Progress toward atomic diagnostics of ultrahigh laser intensities, Phys. Rev. A **99**, 043405 (2019).

[27] I. Yu. Kostyukov and A. A. Golovanov, Field ionization in short and extremely intense laser pulses, Phys. Rev. A **98**, 043407 (2018).

[28] P. H. Bucksbaum, R. R. Freeman, M. Bashkansky, and T. J. McIlrath, Role of the ponderomotive potential in above-threshold ionization, J. Opt. Soc. Am. B **4**, 760 (1987).

[29] D. F. Gordon, J. P. Palastro, and B. Hafizi, Superponderomotive regime of tunneling ionization, Phys. Rev. A **95**, 033403 (2017).

[30] L. W. Pi, S. X. Hu, and A. F. Starace, Favorable target positions for intense laser acceleration of electrons in hydrogen-like, highly-charged ions, Phys. Plasmas **22**, 093111 (2015).

[31] P. J. Prince and J. R. Dormand, High order embedded Runge-Kutta formulas, J. Comput. Appl. Math. **7**, 67 (1981).

[32] M. Tamburini, F. Pegoraro, A. Di Piazza, C. H. Keitel, and A. Macchi, Radiation reaction effects on radiation pressure acceleration, New J. Phys. **12**, 123005 (2010).

[33] M. Tamburini, T. V. Liseykina, F. Pegoraro, and A. MacChi, Radiation-pressure-dominant acceleration: Polarization and radiation reaction effects and energy increase in three-dimensional simulations, Phys. Rev. E **85**, 016407 (2012).

[34] B. Quesnel and P. Mora, Theory and simulation of the interaction of ultraintense laser pules with electrons in vacuum, Phys. Rev. E **58**, 3719 (1998).

[35] A. Maltsev and T. Ditmire, Above Threshold Ionization in Tightly Focused, Strongly Relativistic Laser Fields, Phys. Rev. Lett. **90**, 053002 (2003).

[36] K. I. Popov, V. Y. Bychenkov, W. Rozmus, and R. D. Sydora, Electron vacuum acceleration by a tightly focused laser pulse, Phys. Plasmas **15**, 013108 (2008).

[37] V. Marceau, A. April, and M. Piché, Electron acceleration driven by ultrashort and nonparaxial radially polarized laser pulses, Opt. Lett. **37**, 2442 (2012).

[38] S. Augst, D. Strickland, D. D. Meyerhofer, S. L. Chin, and J. H. Eberly, Tunneling Ionization of Noble Gases in a High-Intensity Laser Field, Phys. Rev. Lett. **63**, 2212 (1989).

[39] Y. Akahane, J. Ma, Y. Fukuda, M. Aoyoma, H. Kiriyama, J. V. Sheldakova, A. V. Kudryashov, and K. Yamakawa, Characterization of wave-front corrected 100 TW, 10 Hz laser pulses with peak intensities greater than 10^{20} W/cm^2, Rev. Sci. Instrum. **77**, 023102 (2006).

[40] A. Link, E. A. Chowdhury, J. T. Morrison, V. M. Ovchinnikov, D. Offermann, L. Van Woerkom, R. R. Freeman, J. Pasley, E.

Shipton, F. Beg, P. Rambo, J. Schwarz, M. Geissel, A. Edens, and J. L. Porter, Development of an in situ peak intensity measurement method for ultraintense single shot laser-plasma experiments at the Sandia Z petawatt facility, Rev. Sci. Instrum. **77**, 10E723 (2006).

[41] A. D. Dichiara, I. Ghebregziabher, R. Sauer, J. Waesche, S. Palaniyappan, B. L. Wen, and B. C. Walker, Relativistic MeV Photoelectrons from the Single Atom Response of Argon to a 10^{19} W/cm^2 Laser Field, Phys. Rev. Lett. **101**, 173002 (2008).

[42] N. Ekanayake, S. Luo, P. D. Grugan, W. B. Crosby, A. D. Camilo, C. V. Mccowan, R. Scalzi, A. Tramontozzi, L. E. Howard, S. J. Wells, C. Mancuso, T. Stanev, M. F. Decamp, and B. C. Walker, Electron Shell Ionization of Atoms with Classical, Relativistic Scattering, Phys. Rev. Lett. **110**, 203003 (2013).